Unveiling Unintentional Fluorine Doping in TMDs During the Reactive Ion Etching: Root Cause Analysis, Physical Insights, and Solution

Kuruva Hemanjaneyulu, Adil Meersha, Jeevesh Kumar, *Member, IEEE*, and Mayank Shrivastava, *Senior Member, IEEE*

***Abstract*— Layered semiconductors, such as transition metal dichalcogenides (TMDs), gained popularity due to their unique properties favoring different applications. For all practical applications, it is essential to have the ability to pattern these layered semiconductors as per the desired dimensions, which are derived from device design or circuit design. Due to its anisotropic nature, plasma or reactive ion etching (RIE) has been the most used technique for patterning bulk semiconductors or thin films. This article unveils the challenges associated with the fluorine-based (SF_6 and CHF_3) plasma etching of TMDs. Subsequently, a detailed root cause analysis is presented with the solution to the problems thereof. We have discovered: 1) high affinity of resists leading to unwanted resist residues over the TMD surface and 2) unintentional doping induced by the fluorine plasma, due to fluorine occupation at the interstitial sites near sulfur (S) defects or its occupation of an S-defect site in the TMD. This was observed despite the surface being masked by the resist. Physical insights were developed using atomic force microscopy (AFM), Raman spectroscopy, electrical characterization, field-effect mobility and transfer length method (TLM)-based contact resistance comparison, and density functional theory (DFT)-based atomistic computations. Furthermore, these insights are used to demonstrate an improved plasma recipe, which mitigates these challenges and allows realization of transistors over a patterned channel while offering characteristic similar to an intrinsic/pristine layer. Finally, the improved plasma recipe, developed for MoS_2, is also shown to be effective for $MoSe_2$, WS_2, and WSe_2 layers.**

***Index Terms*— MoS2, MoSe2, plasma etching, transition metal dichalcogenide (TMD) etching, TMD FET, TMD patterning, WS2, WSe2.**

I. Introduction

ATTRIBUTED to the ultrathin crystal structures, defect-free flat surfaces, high carrier mobilities, bandgap tunability, direct-to-indirect band transition, ability to withstand short-channel effects, and ability to engineer/functionalize surface as per application's need, layered semiconductors, particularly transition metal dichalcogenides (TMDs), have been proven to be the materials for future nanoelectronics, sensing, neuromorphic, and quantum technologies [1]. In general, in all practical device applications using a semiconducting channel, being it CMOS or sensors or neuromorphic, the channel material is required to be patterned in a desired shape or dimension. This often involves plasma or wet etching of the channel material by masking the desired active area using a lithographic mask. For atomically thin layered materials, plasma etching has been a challenge as either the plasma damages the ultrathin and sensitive layered material or the resist may have an affinity toward the atomically thin surface [2]. Wet etching leads to isotropic etching and cannot produce ultrasharp edges, potentially giving rise to edge states [3], [4].

For few-layer TMDs, while there is no literature on defect-free method for active area patterning, for MoS_2, there have been a few initial efforts to etch the material with the intention to thin it down, e.g., using HNO_3-based wet chemistry [4], by dry oxidation of the channel [5], and by exposing MoS_2 to different plasma conditions [6]–[12]. However, it is worth highlighting that none of these techniques were explored in the presence of the resist material over the active area. For patterning monolayer-TMDs, particularly chemical vapour deposition (CVD) MoS_2, oxygen plasma has been an often-used approach [13]; however, it is incredibly time-consuming to pattern few-layer TMD using oxygen plasma. Besides, no report exists on oxygen plasma's impact on channel properties post patterning/etching. A large etching time can also potentially harden the resist and eventually damage the ultrasensitive surface while removing the resist layer. Moreover, hardened resist leaves enough resist residue over the active area, which significantly deteriorates the channel properties. Besides, longer exposure of resists to oxygen plasma is prohibited as the oxygen plasma also etches the often-used resist materials, making the process rather complex. Finally, hard masking is not an option for ultrathin layered materials. Plasma recipes, such as XeF_2 and CF_4, have also been reported with low etch rates, leading to similar issues such as oxygen plasma. In summary, a technique to etch TMD layers, particularly in presence of masking resist and without impacting the TMD layer adversely, is still missing.

Manuscript received January 2, 2022; revised February 9, 2022; accepted February 14, 2022. Date of publication March 9, 2022; date of current version March 28, 2022. This work was supported by the NNetRA Program of Ministry of Electronics and Information Technology (MeitY), Department of Science and Technology (DST), and the Ministry of Education, formerly the Ministry of Human Resource Development (MHRD), Government of India. The review of this article was arranged by Editor A. M. P. Anantram. *(Corresponding author: Mayank Shrivastava.)*

The authors are with the Department of Electronic Systems Engineering, Indian Institute of Science, Bengaluru 560012, India (e-mail: mayank@iisc.ac.in).

Color versions of one or more figures in this article are available at https://doi.org/10.1109/TED.2022.3152459.

Digital Object Identifier 10.1109/TED.2022.3152459

Keeping in mind these gaps, a plasma etch technique is required to be developed while ensuring that the etch chemistry does not perturb the active area physically or chemically. This article presents the patterning of various TMDs through electron-beam lithography while investigating different fluorine chemistries. Choice of fluorine chemistry is attributed to its high reactivity and a faster etch rate. Two specific combinations of fluorine plasma, i.e., SF_6 [11], and for the first time, CHF_3, are investigated with a target to pattern multilayered MoS_2. Besides, this article addresses the following three significant issues associated with plasma etching while developing physical insights using experiments and density functional theory (DFT)-based computations: 1) resist affinity toward the ultrathin surface leading to resist residues; 2) chemical doping of the active area induced by plasma exposure through the resist; and 3) crystal damage due to ion diffusion through the resist and its sidewalls. The reported chemistry/process has been further optimized to eliminate these issues. Finally, the developed chemistry is validated for other TMDs, which generalizes the applicability of the proposed approach.

II. Experimental and Computational Approach

Back-gated TMD devices were realized using electron-beam lithography to study the impact of plasma-based patterning techniques on the resulting active area's physical, chemical, and electrical properties. Large TMD flakes were mechanically exfoliated over a cleaned SiO_2(90 nm)/Si(p^+) substrate. Flakes with the desired thickness of ≈10 nm were identified using a high-resolution optical microscope and atomic force microscopy (AFM). For patterning, two layers of polymethyl methacrylate (PMMA), one sensitive thick bottom layer, followed by a less sensitive thin top layer, were spin-coated over the sample. Post-electron-beam lithography (exposure), PMMA patterns were developed using the MIBK:IPA solution. The sample was then exposed to reactive ion plasma inside a reactive ion etching (RIE) chamber to etch out TMD from the undesired regions. Subsequently, source/drain contacts were formed using the electron-beam lithography and liftoff process followed by a soft anneal. The flakes were characterized through AFM and Raman spectroscopy in the intermediate steps to assess the change in the channel quality and closely analyze the presence of damage or residues. All the devices were characterized electrically inside a cryogenic vacuum probe station while maintaining vacuum below 10^{-4} torr across all measurements. While the back-gated TLM structures with channel lengths 0.3, 0.5, 0.8, 1.0, and 1.2 μm were realized, for comparison, the shortest channel length device (0.3 μm) was used unless mentioned exclusively.

III. RIE of TMDs: The Problems at Hand

A. SF_6 Chemistry: Affinity to Resist Layers

SF_6 chemistry was a natural choice, to begin with, attributed to the selectivity it offers between the target material to etch (TMD) and substrate (SiO_2) beneath it. SF_6 was earlier reported to etch MoS_2 without any significant removal of SiO_2 beneath. SF_6 plasma follows the following etch chemistry:

$$MoS_2 + 4SF_6 \rightarrow MoF_4 + 2SF_6 + 2SF_4. \quad (1)$$

By-products of this chemistry, i.e., MoF_4, SF_4, and SF_6, are volatile and swept away without leaving any residue [11]. It should also be noted that SF_6 will also partially etch PMMA.

Etching of MoS_2 flakes using this chemistry on bare samples, such as reported earlier for thinning MoS_2 flakes [8], [11], revealed approximate etch rates of more than 2 nm/s. The same did not follow when resists were used to mask a certain region. Fig. 1(a) shows a high-resolution optical microscope image of one of the back-gated devices with 0.3-μm channel length. Rectangles drawn in Fig. 1(b) depict the regions that were partially blocked using PMMA, whereas the channel region (the region between S/D metal) was completely blocked by PMMA. While the SF_6 plasma is not expected to etch SiO_2, however, the region inside the rectangles in Fig. 1(b) depict uneven contrast. This difference has been probed using AFM, as shown in Fig. 1(b)–(f). Fig. 1(b) shows the corresponding AFM scan of the entire area, whereas Fig. 1(c)–(e) shows the zoomed-in high-resolution scans of areas marked with white rectangles in (b). All the scans display different contrast regions seen in the optical image with clear boundaries. Plots numbered (1)–(5) of Fig. 1(f) present the line plots along the white dashed lines marked in Fig. 1(c)–(e). All the line plots depict a dip of approximately ≈3 nm at the boundary of the patterned rectangle. This dip demarks the regions with different contrasts. Post this dip, the surface roughness was found to be significantly higher (7 nm), which is attributed to the residue generated by the reaction of plasma with PMMA/MoS_2, which was redeposited inside the open regions.

To further probe this, back-gated transistors have been characterized electrically. A comparison of input characteristics of devices released over patterned flakes (SF_6 etch) and flakes without patterning (pristine) is presented in Fig. 2. SF_6 etch devices depict very low ON currents and high OFF-state leakage than the pristine back-gated devices. Lower ON currents imply the residue at the metal–MoS_2 interface for the devices over the patterned flakes. Residue adds an unwanted barrier at the metal–semiconductor interface, lowering carrier injection significantly. It is attributed to fluorine and sulfur radicals' reaction with the bottom layer of PMMA at the PMMA/SiO_2 interface forming a thin layer of ≈3 nm. The same reaction with PMMA at the interface of PMMA/MoS_2 creates a barrier layer of thickness ≈3 nm for carriers crossing the interface, thereby reducing the ON currents drastically.

The SF_6 etch chemistry is, therefore, not an affordable process when used in conjunction with resists mask. The residue below the S/D contacts can be eliminated by patterning the MoS_2 flake after the deposition of contact metals, as reported by Kotekar-Patil *et al.* [14]. However, the residue inside the channel region can still influence the top dielectric growth, channel mobility, and gate-stack yield. Therefore, patterning through a plasma process, without leaving residues and without degrading the channel properties, becomes mandatory. To address this, another plasma process with the same fluorine

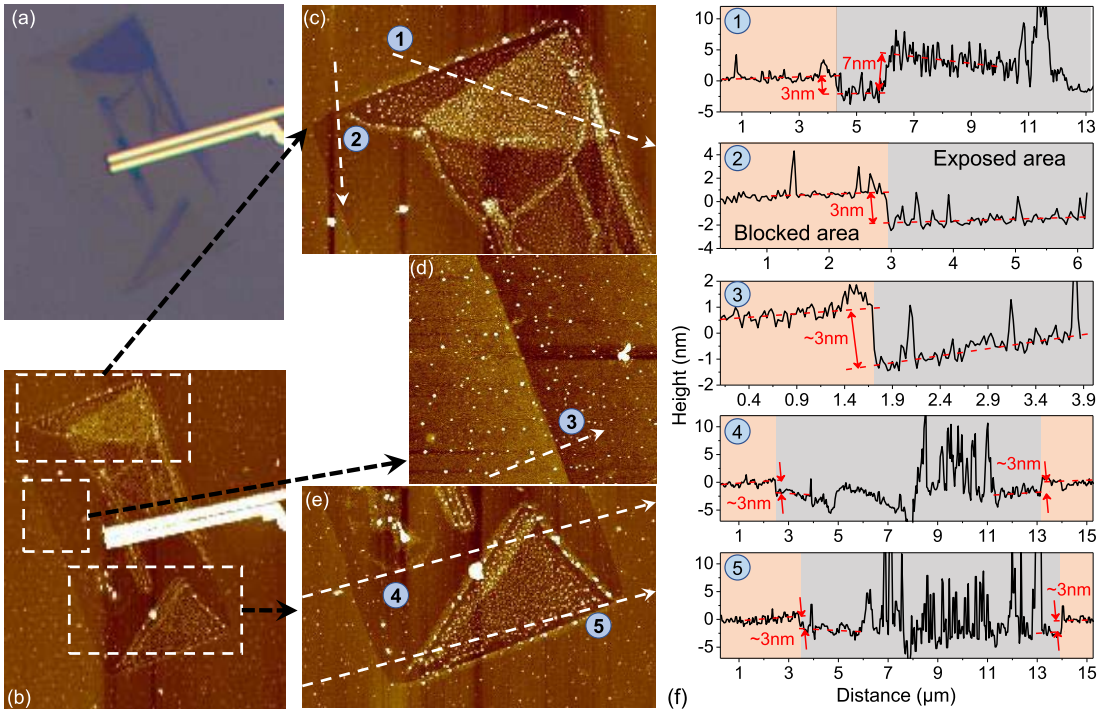

Fig. 1. Atomic microscopy analysis of rectangular pattern of size 10 μm $\times$ 20 μm consisting of patterned flake. (a) Optical image describing the contrast differences inside and outside the rectangular patterned area along with the presence of postetch residues. (b) Corresponding AFM scan of the area. (c)–(e) Zoomed-in high-resolution scans of the areas marked with the white dotted rectangles in (b). (1)–(5) of (f) are the line plots taken along the white dotted lines marked in the zoomed-in scan areas.

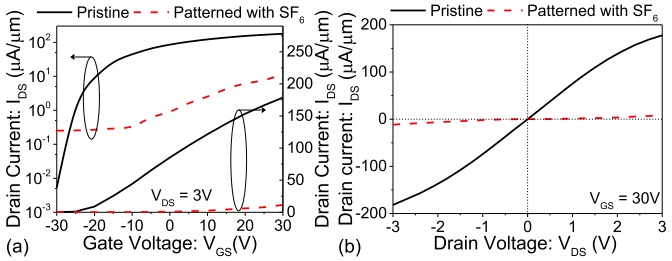

Fig. 2. Comparison of electrical characteristics of the devices over patterned flakes using SF_6 plasma and devices fabricated over flakes without patterning. (a) Input characteristics and (b) output characteristics.

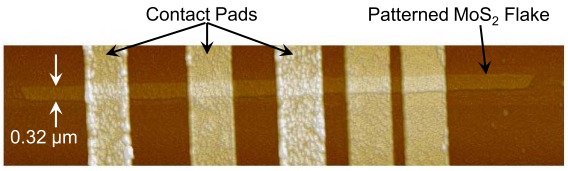

Fig. 3. AFM scan of a device fabricated over a patterned flake using CHF_3 plasma.

chemistry is being explored and presented in the following subsection.

B. CHF_3 Chemistry: Unintended F–Doping?

In this section, we would assess the ability of CHF_3 plasma to etch MoS_2 without adding to postetch residue. CHF_3 plasma is less reactive than SF_6 plasma, and therefore, CHF_3 plasma is expected to avoid postetch residue issues (in presence of resist) as observed in the previous section. On the other hand, CHF_3 plasma chemistry is the same as SF_6 plasma, and hence, the etch behavior must not drift significantly.

Similar to the SF_6 plasma, initial experiments are conducted on an unmasked sample followed by a high-resolution optical microscopy analysis. As predicted, the chemistry has shown lesser etch rates, i.e., etching thinner flakes of thickness ≈6 nm in 15 s and 50 nm in 2 min (the same for SF_6 plasma was 6 nm in 5 s and 50 nm in 30 s). Relatively lower etch rates with linear etch depth with time offer a far better control over the etching process.

Similar to SF_6 plasma, qualitative experiments to investigate postetch residues were carried out by fabricating back-gated devices on MoS_2 flakes patterned using CHF_3 plasma. The characteristics were compared with back-gated FET on flakes without patterning. The AFM scan of patterned flake and a TLM sample realized over the patterned flake is shown in Fig. 3. AFM scan confirms the absence of postetch residue as earlier seen for SF_6 plasma (see Fig. 1). A comparison of input and output characteristics of this device with the device over an intrinsic flake (flake without patterning) is presented in Fig. 4. Fig. 4(a) shows a negative shift in the threshold voltage, higher OFF-state (S/D leakage) current, degradation of the subthreshold slope (weaker gate control), and around 50% drop in ON-current. The output characteristics depict the ohmic behavior of the contacts with symmetric conduction, similar to the pristine devices, highlighting the

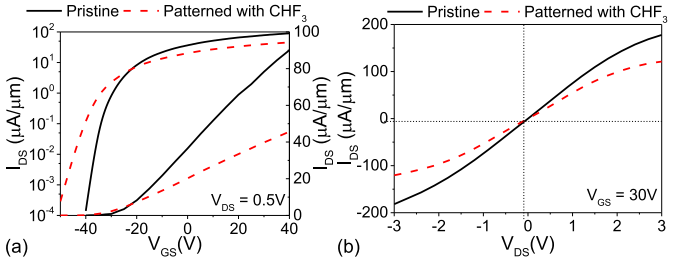

Fig. 4. Comparison of electrical characteristics of the devices over patterned flakes using CHF_3 plasma and devices fabricated over flakes without patterning. (a) Input characteristics and (b) output characteristics. Both the TMD layers (pristine and patterned) were chosen to be of same thickness.

absence of any physical residue at the metal–semiconductor interface unlike seen in SF_6 plasma case. A high OFF-state leakage with negative shift in threshold voltage signifies the creation of new donor-like states (or n-type doping) over the patterned MoS_2 flake. Lower ON-current without affecting the contact behavior signifies drop in carrier mobility, possibly due to impurity scattering caused by added dopants (or donor states) and/or compressive strain introduced in the 2-D layer [15] from the fluorine plasma. A similar kind of doping and introduction of strain was earlier reported in case of N_2 plasma [16]. Degraded subthreshold slope also signifies n-type doping of the channel. These hypotheses/claims, however, are required to be validated to probe the root cause of the observed degradation in transistor performance. This has been addressed in the next section.

IV. F–Doping: Pathways, Root Cause Analysis, and Solution

A. Root Cause Analysis

Increased leakage and poor subthreshold slopes for the patterned devices can be attributed to the doping caused by the plasma process [17]–[19]. The doping mechanism attributed to plasma exposure is, however, not well understood.

Fig. 5 shows possible pathways for the plasma (in this case fluorine) radicals to reach the masked active region. In case of SF_6 plasma, its high diffusivity and high reactivity lead to the formation of a thin residue layer over the entire surface of MoS_2, which resulted in a significant residue leftover as seen earlier. For CHF_3 plasma, low reactivity and diffusivity have resulted in rather controlled etch rates causing no residue layer at the interface. However, the fluorine radicals reached via the diffusion process and may have doped the MoS_2 layer. Besides the diffusion through the MoS_2–PMMA (bottom layer) interface, depicted by dashed blue arrows in Fig. 5, the fluorine radicals can also diffuse through the PMMA layer, as shown by red arrows in Fig. 5, and dope the MoS_2 layer. To dope MoS_2, these fluorine radicals may occupy an interstitial site or may occupy a chalcogen vacancy site. This has been explained and explored further in this section.

However, before we investigate the role of fluorine radicals at the interstitial site and the chalcogen vacancy site, it is worth confirming the presence of doping using experimental means. To confirm the doping as explained above, devices

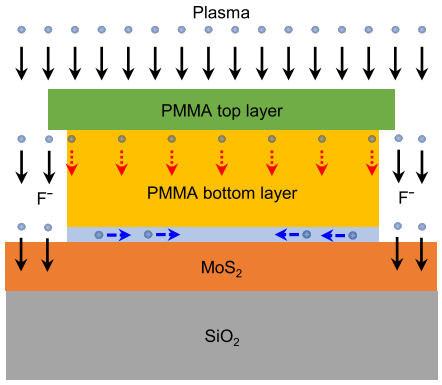

Fig. 5. Schematic representation depicting possible diffusion pathways for the fluorine radicals (depicted by blue spheres) causing fluorine radicals to reach masked MoS_2 layer: 1) via MoS_2-PMMA (bottom layer) interface, depicted by dashed blue arrows, and 2) through PMMA mask, depicted by dashed red arrows.

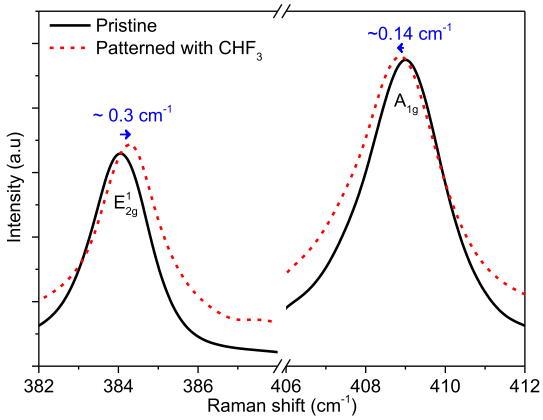

Fig. 6. Comparison of Raman spectra across patterned and intrinsic flakes. Patterned flakes show relative shifts in both A_{1g} and E^1_{2g} peaks signifying, doping, and compressive strain for the patterned flakes.

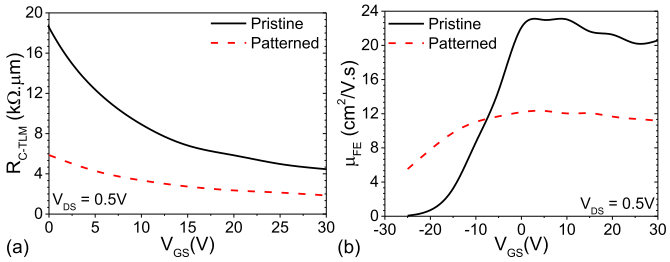

Fig. 7. Comparison of (a) contact resistance and (b) field-effect mobility of the devices over patterned flakes using CHF_3 plasma and devices fabricated over flakes without patterning. Here, the contact resistance is extracted using the transfer length method (TLM).

are characterized by the Raman spectroscopy. Raman spectra extracted from the patterned and intrinsic flakes are compared in Fig. 6. A_{1g} and E^1_{2g} peaks in the spectra extracted for the patterned flakes, when compared to intrinsic flakes, show a relative shift. A shift in A_{1g} peak of ≈ -0.14 cm^{-1} confirms the presence of n-type doping [20]. A relatively smaller shift corresponds to lower doping concentration, which correlates with the I–V characteristics depicting relatively lower negative shift by noticeable ON current degradation, which can be

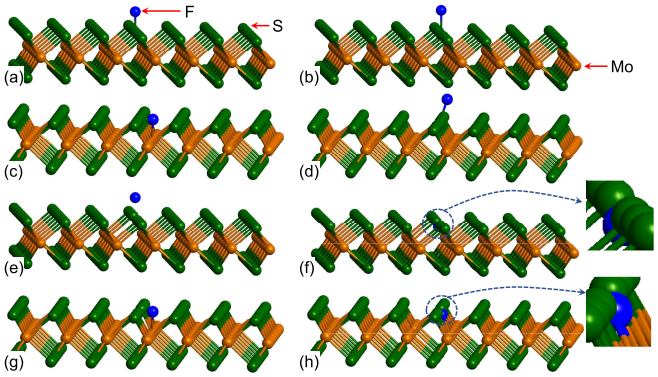

Fig. 8. Atomic analysis for minimum energy states (post structural optimization or energy relaxation computation) for fluorine atoms as surface adsorbent and as interstitial. Fluorine as adsorbent over pristine MoS_2 crystal (a) before and (b) after optimization for minimum energy state. Fluorine as interstitial over pristine MoS_2 crystal (c) before and (d) after optimization for minimum energy state. Fluorine as adsorbent over sulfur defected MoS_2 crystal (e) before and (f) after optimization for minimum energy state. Fluorine as interstitial over sulfur defected MoS_2 crystal (g) before and (h) after optimization for minimum energy state.

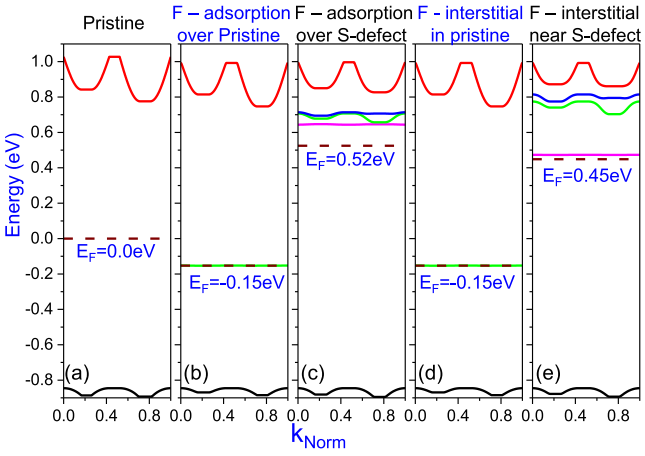

Fig. 9. Effect of fluorine as adsorbent/interstitial on the band structure of MoS_2 crystal (a) pristine crystal, (b) with fluorine adsorbed over pristine MoS_2 crystal, (c) with fluorine adsorbed over S defect, (d) with fluorine as adsorbent/interstitial in pristine MoS_2 crystal and (e) with fluorine interstitial near S-defect of MoS_2. Here, k_{Norm} ranges from 0 to 1, with the symmetry points Γ, M, L, A, Γ, K, H, and A located at 0, 0.167, 0.26, 0.428, 0.52, 0.714, 0.806, and 1.0, respectively.

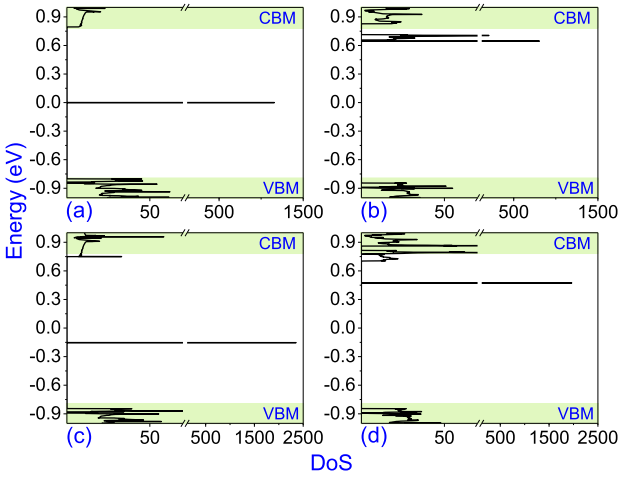

Fig. 10. Comparison of density of states (DoS) for different crystal configurations studied. (a) Fluorine atom adsorption over pristine MoS_2 crystal, (b) fluorine atom adsorption over S-defect in MoS_2 crystal, (c) fluorine interstitial atom in pristine MoS_2 crystal, and (d) fluorine interstitial atom near S-defect in MoS_2 crystal.

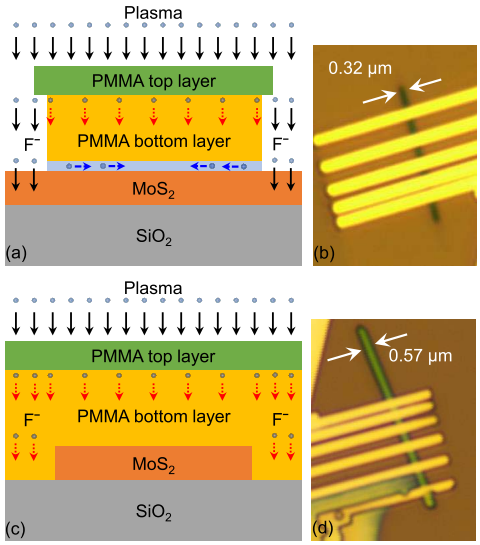

Fig. 11. Two different sets of test structures realized over the same wafer, for probing the pathways for the fluorine atoms causing doping of MoS_2 layer. (a) and (b) Devices realized on layers that were intentionally patterned and (c) and (d) devices realized on rectangular flakes (flakes that are relatively uniform in width) while keeping it masked by PMMA from all the sides during the plasma process.

attributed to increased impurity scattering. The shift in E^1_{2g} of $\approx$0.3 cm^{-1} confirms a mild compressive strain introduced into the 2-D layer [15], which also leads to a drop in carrier mobility [15]. A similar kind of doping and introduction of strain was earlier reported in case of N_2 plasma [16].

Raman results (the presence of doping and compressive strain) imply that the type of doping can only be substitutional. Unlike surface charge transfer doping, where the dopants get adsorbed on the surface via charge transfer, dopants in substitutional doping replace/occupy atomic/empty sites in the crystal. This substitutional doping is attributed to the substitution of fluorine atoms [17].

To further validate the presence of doping and strain, we have compared contact resistance and field-effect mobility for cases with and without plasma. The assumption/hypothesis is that if fluorine radicals cause n-type doping (as shown from Raman), then the contact resistance of devices with fluorine plasma must be lower. Also, if fluorine radicals have resulted in compressive strain (as shown from Raman data), then the field-effect mobility of devices with plasma exposure must be lower than devices without plasma exposure. Fig. 7(a) and (b) confirms these.

B. F–Doping: Physical Insights

It is worth investigating the nature and role of fluorine radicals as dopants, which is explored using the DFT-based band structure and density of states computations using quantum-wise Atomistix ToolKit (ATK) [21], [22]. Energy optimization

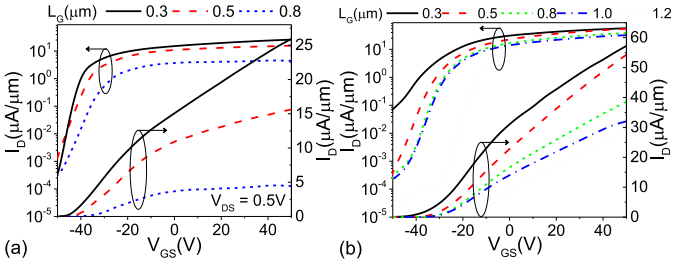

Fig. 12. Input characteristics comparison of (a) patterned device and (b) masked devices.

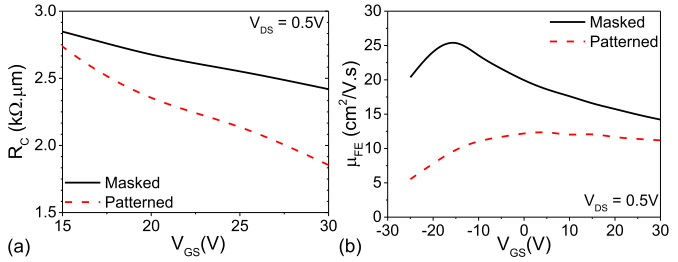

Fig. 13. (a) Contact resistance and (b) field-effect mobility comparison of devices realized over a patterned layer (using CHF_3 plasma) and devices realized over a rectangular MoS_2 layer, which was masked through PMMA during the plasma process. Here, the contact resistance is extracted using the transfer length method (TLM).

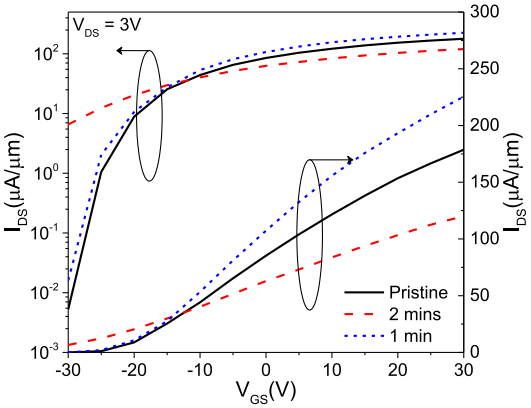

Fig. 14. Input characteristics comparison of devices realized over a pristine layer (without exposing to plasma process, however keeping rest of the process identical) and over patterned layer with different plasma exposure times. All the TMD layers, used for this comparison, were chosen to be of the same thickness.

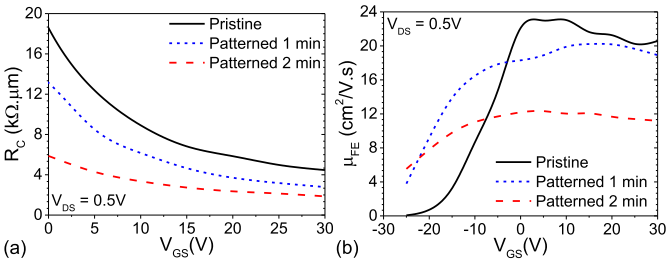

Fig. 15. (a) Contact resistance and (b) field-effect mobility comparison of devices realized over patterned layers (patterned device) while keeping different plasma exposure times and devices realized over a rectangular MoS_2 layer without exposing it to the plasma process (pristine device). The rest of the process was kept identical. Here, the contact resistance is extracted using the transfer length method (TLM).

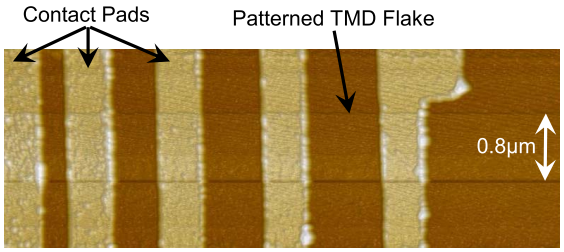

Fig. 16. AFM map of one of the patterned device, realized over other TMD layers.

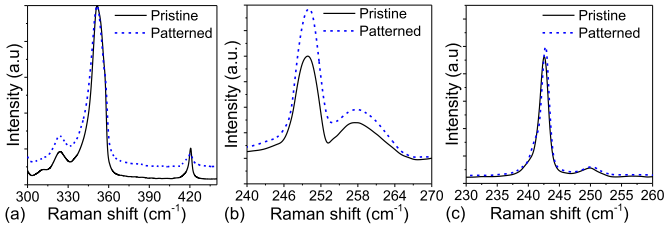

Fig. 17. Comparison of Raman spectra across intrinsic and patterned layers of different transition metal dichalcogenides. (a) WS_2, (b) WSe_2, and (c) $MoSe_2$. The spectra depict no shift in respective peaks, confirming the absence/negligible amount of unintended F-doping when an optimized recipe was used.

was done with 0.01-eV/Å force and 0.001-eV/Å^3 energy cutoffs. Perdew–Burke–Ernzerhof (PBE) form of generalized gradient approximation (GGA) functional with Grimme-D2 Van der Waals (vdW) correction was incorporated to capture long-range vdW interactions. Due to an extremely low energy and density plasma, the dopants (fluorine radicals) are expected to occupy an interstitial site and sulfur vacancy sites rather than replacing the sulfur atom from the crystal [17].

Fig. 8 shows various atomic configurations possible in terms of fluorine radical's placement at different adsorption/interstitial sites in the 2-D TMD crystal. Here, a 7×7 unit cell of MoS_2, with and without sulfur defect, is considered for computational studies. Before band structure and density of states computations, these structures were optimized for each atom to achieve a low energy state, which is required to estimate the exact positions of adsorption and interstitial and substitutional sites for the fluorine atom.

Band structure (see Fig. 9) and density of states (see Fig. 10) plots show that S-defect alone is observed to introduce inevitable n-type doping with a shift of Fermi level by ≈0.25 eV. For the case of fluorine adsorption/interstitial over pristine MoS_2, a shift of approximately ≈0.15 eV toward the valence band is observed. This corresponds to p-type doping and, however, is less influencing as n-doping is already present with S-defect naturally. Without S-defect, fluorine atom adsorbed over MoS_2 crystal or sitting at an interstitial site creates a state near $E = 0$, which does not affect the electrical properties of the crystal. However, fluorine atom as adsorbent/interstitial near sulfur defect makes fluorine atom a substitutional n-type dopant, with high density of state of

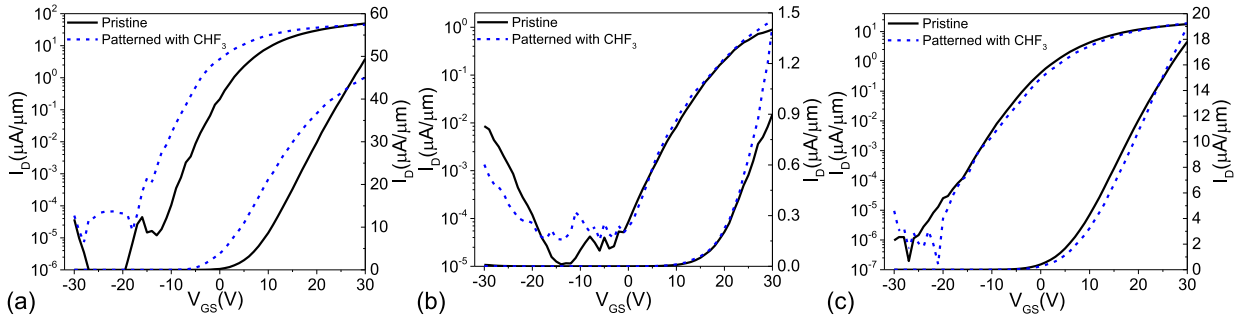

Fig. 18. Drain current versus gate voltage characteristics of FETs realized over intrinsic and patterned layers of different transition metal dichalcogenides. (a) WS_2, (b) WSe_2, and (c) $MoSe_2$. The overlapping characteristics confirm the absence of unintended F-doping when an optimized recipe was used. Both the TMD layers (pristine and patterned) were chosen to be of same thickness.

the introduced shallow donor state. Band structure of this replacement reveals midgap states closer to the conduction band (shallow donor state), which results in a further shift of the Fermi level closer to the conduction band. It amounts to a shift of approximately ≈0.52 eV, introducing relatively very strong n-type doping compared to doping caused by natural S-defect. Such a shift in Fermi level is responsible for a negative threshold voltage shift along with high OFF-state S/D leakage observed across these devices. Crystal optimization (energy relaxation computation) and band structure analysis concludes and confirms the n-type doping only due to fluorine radicals (with sufficient energy), which occupies thermodynamically favorable sulfur defect sites or interstitial sites near sulfur defects.

C. Pathways for F− Radicals

While we have confirmed the presence of doping and compressive strain attributed to substitutional doping caused by the Fluorine atoms, the pathway for it to reach the MoS_2 layer is still not clear. This is worth addressing to probe the root cause and solve the unintended doping issues. Fig. 5 shows possible pathways for the fluorine radicals to reach the masked active region. To decouple the two pathways, we have realized two special test structures, as shown in Fig. 11. In one case, the MoS_2 layer was intentionally patterned, allowing fluorine radicals to diffuse through the MoS_2–PMMA (bottom layer) interface as well as PMMA layers. Fig. 11(a) and (b) shows the schematic representation and optical view, respectively, of the "patterned device." In the other case, a rectangular flake was chosen on the same wafer, and it was covered using PMMA from all sides such that there was no possibility of fluorine radicals to diffuse through the MoS_2–PMMA (bottom layer) interface. Fig. 11(c) and (d) shows the schematic representation and optical view, respectively, of the "masked device."

Fig. 12 compares the input characteristics of patterned and masked devices for different channel lengths. Compared to the input characteristics of the pristine device, presented in Fig. 4, ON current, subthreshold slope, OFF-state leakage, and threshold voltage can be seen to be degraded in both masked and patterned device cases. The degradation, attributed to unintentional F-doping, is, however, lower in case of masked device when compared to the patterned device. This signifies higher diffusion of F-radicals through the PMMA–MoS_2 interface than the diffusion through the PMMA layer directly. A difference in the strength of doping in these two cases is further validated by extracting contact resistance and field-effect mobility of patterned and masked devices, as shown in Fig. 13. Compared to the pristine device's contact resistance and mobility, as shown earlier in Fig. 7, here, both the patterned and masked devices were found to have lower contact resistance [see Fig. 13(a)] and mobility [see Fig. 13(a)]. The contact resistance and field-effect mobility for the patterned device were found to be lower than the same of masked device. This further confirmed, as explained above, higher F-doping in the patterned device when compared to the masked device.

D. Solution to the Problem

It is clear at this stage that high F-doping has an adverse effect on the device's performance, and therefore, an optimum exposure time/power combination is required for the complete etch of TMD layers while avoiding unintended F-doping. This required further optimization to lower the etch time. Fig. 14 shows the input characteristics of devices with different plasma exposure times and compared it with pristine device's characteristics. Fig. 14 shows that while a 2-min exposure resulted in degraded characteristics (lower ON current, higher OFF current, lower threshold voltage, and so on), limiting the exposure time to 1 min offered improved ON current with a minor/negligible threshold voltage shift. Improved ON current can be explained by moderate F-doping, which lowered the contact resistance, as shown in Fig. 15(a), without any observable compromise in the field-effect mobility [see Fig. 15(b)]. In case of 2 min of plasma exposure time, degraded characteristics are attributed to a significant increase in F-doping, which corroborates with earlier explanations and is confirmed through the significant drop on field-effect mobility and contact resistance, as shown in Fig. 15.

V. Validation for Other TMDs

The optimized plasma recipe, as discussed above, has resulted in no residue formation and negligible doping. Its applicability is therefore investigated for the other conventional TMDs, such as WS_2, WSe_2, and $MoSe_2$, to generalize the findings and applicability of this work. We found slightly different etch rates for different TMDs, which is attributed to lower reactivity of W-based TMDs with fluorine plasma

than Mo-based TMDs. MoS_2 and $MoSe_2$ had same etch rates. The same was true for WS_2 and WSe_2. For further validation, transistors were realized over an intrinsic layer and patterned layer, as explained in the previous sections. "Pristine" devices were not exposed to the plasma process, whereas "patterned" devices were realized over TMD layers patterned using the optimized plasma recipe. Fig. 16 shows the well-patterned layer without any residue residing over the active area. Raman spectroscopy of pristine and patterned channel, as shown in Fig. 17, shows no shift in respective peaks, which signifies the absence of unintended F-doping. Subsequently, input characteristics, as shown in Fig. 18, show almost identical drain current versus gate voltage characteristics with similar ON and OFF currents. This validates the applicability of the presented findings above for other conventional TMDs.

VI. Conclusion

In this work, the patterning of few-layer, single-crystal TMDs using fluorine-based (SF_6 and CHF_3) plasma chemistry is successfully examined to achieve the desired dimensions. SF_6 plasma, which offered a faster TMD etch, resulted in significant resist residue over the masked TMD layers. This was attributed to the high reactivity of SF_6 plasma and higher diffusivity of F-radicals through the resist-TMD interface. This caused significant channel degradation as seen from a substantial drop in ON current and a significant increase in OFF current. On the other hand, CHF_3 plasma was found to offer a well-controlled etch with a relatively lower etch rate than SF_6 plasma. While no resist residue was found in this case, CHF_3 plasma caused significant fluorine doping due to the diffusion of F-radicals from the PMMA-TMD interface and through the PMMA layer. The presence of doping was confirmed using the Raman spectroscopy and TLM-based contact resistance extraction. The F-doping also resulted in a compressive strain across the material, as observed from the Raman spectroscopy, which we confirmed through field-effect mobility extraction. We found the presence of doping lowered the field-effect mobility and contact resistance. A direct correlation between the extent of doping, contact resistance, and field-effect mobility was seen, i.e., the higher the doping, the lower the mobility and contact resistance. Mobility degradation due to the unintentional doping, however, dominated the transistor characteristics, causing reduced ON current with increased OFF-state current. The exact nature of doping by F-atoms was modeled/explored using DFT-based atomistic computations. We found that the F-atoms result in shallow donor traps when they occupy an S-defect site or an interstitial site near S-defect. Otherwise, F-doping was found to be relatively neutral. Through the systematic design of experiments, extraction of I–V data, field-effect mobility, and contact resistance, we also revealed that the doping is contributed through two routes, i.e., PMMA–TMD interface and through the PMMA layer. In contrast, the contribution of the PMMA-TMD interface was higher. Finally, these insights are used to demonstrate an improved plasma recipe that mitigates these challenges and allows the realization of transistors over a patterned channel while offering characteristics similar or better to an intrinsic/pristine layer. The improved plasma recipe, developed for MoS_2, is also shown to be effective for $MoSe_2$, WS_2, and WSe_2 layers.

References

[1] M. Shrivastava and V. R. Rao, "A roadmap for disruptive applications and heterogeneous integration using two-dimensional materials: State-of-the-art and technological challenges," *Nano Lett.*, vol. 21, no. 15, pp. 6359–6381, 2021, doi: 10.1021/acs.nanolett.1c00729.

[2] K. Brenner and R. Murali, "Single step, complementary doping of graphene," *Appl. Phys. Lett.*, vol. 96, no. 6, Feb. 2010, Art. no. 063104, doi: 10.1063/1.3308482.

[3] X. Xi, J. Ma, S. Wan, C.-H. Dong, and X. Sun, "Observation of chiral edge states in gapped nanomechanical graphene," *Sci. Adv.*, vol. 7, no. 2, Jan. 2021, Art. no. eabe1398.

[4] K. K. Amara, L. Chu, R. Kumar, M. Toh, and G. Eda, "Wet chemical thinning of molybdenum disulfide down to its monolayer," *APL Mater.*, vol. 2, no. 9, Sep. 2014, Art. no. 092509, doi: 10.1063/1.4893962.

[5] M. Yamamoto, T. L. Einstein, M. S. Fuhrer, and W. G. Cullen, "Anisotropic etching of atomically thin MoS_2," *J. Phys. Chem. C*, vol. 117, no. 48, pp. 25643–25649, Dec. 2013, doi: 10.1021/jp410893e.

[6] F. Zhang, C.-H. Lee, J. A. Robinson, and J. Appenzeller, "Exploration of channel width scaling and edge states in transition metal dichalcogenides," *Nano Res.*, vol. 11, no. 4, pp. 1768–1774, Apr. 2018, doi: 10.1007/s12274-017-1794-x.

[7] T. Lin *et al.*, "Controlled layer-by-layer etching of MoS_2," *ACS Appl. Mater. Interfaces*, vol. 7, no. 29, pp. 15892–15897, Jul. 2015, doi: 10.1021/acsami.5b03491.

[8] M. H. Jeon *et al.*, "Controlled MoS_2 layer etching using CF_4 plasma," *Nanotechnology*, vol. 26, no. 35, Aug. 2015, Art. no. 355706, doi: 10.1088/0957-4484/26/35/355706.

[9] K. S. Kim *et al.*, "Atomic layer etching mechanism of MoS_2 for nanodevices," *ACS Appl. Mater. Interfaces*, vol. 9, no. 13, pp. 11967–11976, Apr. 2017, doi: 10.1021/acsami.6b15886.

[10] C. H. Lee *et al.*, "A self-limiting layer-by-layer etching technique for 2H-MoS_2," *Appl. Phys. Exp.*, vol. 10, no. 3, p. 035201, Feb. 2017, doi: 10.7567%2Fapex.10.035201.

[11] S. Xiao *et al.*, "Atomic-layer soft plasma etching of MoS_2," *Sci. Rep.*, vol. 6, no. 1, p. 19945, Jan. 2016, doi: 10.1038/srep19945.

[12] Y. Huang *et al.*, "An innovative way of etching MoS_2: Characterization and mechanistic investigation," *Nano Res.*, vol. 6, no. 3, pp. 200–207, Mar. 2013, doi: 10.1007/s12274-013-0296-8.

[13] L. Yu *et al.*, "Enhancement-mode single-layer CVD MoS_2 FET technology for digital electronics," in *IEDM Tech. Dig.*, Dec. 2015, p. 32.

[14] D. Kotekar-Patil, J. Deng, S. L. Wong, C. S. Lau, and K. E. J. Goh, "Single layer MoS_2 nanoribbon field effect transistor," *Appl. Phys. Lett.*, vol. 114, no. 1, Jan. 2019, Art. no. 013508, doi: 10.1063/1.5079860.

[15] D. Lloyd *et al.*, "Band gap engineering with ultralarge biaxial strains in suspended monolayer MoS2," *Nano Lett.*, vol. 16, no. 9, pp. 5836–5841, Sep. 2016, doi: 10.1021/acs.nanolett.6b02615.

[16] A. Azcatl *et al.*, "Covalent nitrogen doping and compressive strain in MoS_2 by remote N_2 plasma exposure," *Nano Lett.*, vol. 16, no. 9, pp. 5437–5443, Sep. 2016, doi: 10.1021/acs.nanolett.6b01853.

[17] S.-S. Chee, H. Jang, K. Lee, and M.-H. Ham, "Substitutional fluorine doping of large-area molybdenum disulfide monolayer films for flexible inverter device arrays," *ACS Appl. Mater. Interfaces*, vol. 12, no. 28, pp. 31804–31809, Jul. 2020, doi: 10.1021/acsami.0c07824.

[18] S. Wi *et al.*, "Enhancement of photovoltaic response in multilayer MoS_2 induced by plasma doping," *ACS Nano*, vol. 8, no. 5, pp. 5270–5281, May 2014, doi: 10.1021/nn5013429.

[19] A. Nipane, D. Karmakar, N. Kaushik, S. Karande, and S. Lodha, "Few-layer MoS_2 p-type devices enabled by selective doping using low energy phosphorus implantation," *ACS Nano*, vol. 10, no. 2, pp. 2128–2137, Feb. 2016, doi: 10.1021/acsnano.5b06529.

[20] D. Kiriya, M. Tosun, P. Zhao, J. S. Kang, and A. Javey, "Air-stable surface charge transfer doping of MoS_2 by benzyl viologen," *J. Amer. Chem. Soc.*, vol. 136, no. 22, pp. 7853–7856, Jun. 2014, doi: 10.1021/ja5033327.

[21] J. M. Soler *et al.*, "The SIESTA method forab initioorder-nmaterials simulation," *J. Phys., Condens. Matter*, vol. 14, no. 11, pp. 2745–2779, Mar. 2002, doi: 10.1088/0953-8984/14/11/302.

[22] M. Brandbyge, J.-L. Mozos, P. Ordejón, J. Taylor, and K. Stokbro, "Density-functional method for nonequilibrium electron transport," *Phys. Rev. B, Condens. Matter*, vol. 65, Mar. 2002, Art. no. 165401, doi: 10.1103/PhysRevB.65.165401.